Dispersive Resonance Modulation Based on the Mode-Coupling Effect in a Capacitive Micromechanical Resonator

Kuo Lu,[1] Kai Wu,[1] Qingsong Li,[1,2,*] Xin Zhou,[1,2] Yongmeng Zhang,[1,2] Xiang Xi,[1,2] Xuezhong Wu,[1,2,3] and Dingbang Xiao[1,2,3,†]

[1] *College of Intelligence Science, National University of Defense Technology, Changsha 410073, China*
[2] *Hunan MEMS Research Center, Changsha, China*
[3] *Laboratory of Science and Technology on Integrated Logistics Support, National University of Defense Technology, Changsha 410073, China*

(Received 20 April 2022; revised 25 June 2022; accepted 25 July 2022; published 2 September 2022)

This paper presents a theoretical and experimental investigation into the electrostatic coupling mechanism between different nonlinear modes inside a single resonator. Nonlinear intermodal coupling allows an arbitrary mode to be used as a modulator for the resonance of the coupled mode, presenting an efficient method to tune the frequency of a specific vibration mode. Here, a capacitive micromechanical resonator is developed, in which different modes exhibit different nonlinear characteristics. Inside this resonator, interactions between different nonlinear modes induced by electrostatic fields are observed and accurately modeled. It demonstrates that resonance modulation control can be achieved by activating the coupled modes based on the dispersive parametric coupling effect. Meanwhile, the resonance modulation is jointly determined by coupled modes, providing a theoretical basis and approach for modal manipulation technology. The dispersive coupling between intrinsic modes enables the probe resonance to be tuned by nearly 100 times its bandwidth, and its range and polarity can also be controlled by selecting the resonance of the pump mode. It is proven that resonance modulation control induced by the modal coupling effect can efficiently tune the resonator's resonance frequency over a wide range, which presents a promising voltage-frequency transduction scheme with high sensitivity and low noise for the precision instrument. Its pull range exhibits a great potential of more than 20% as a voltage-controlled oscillator and can be customized to satisfy different requirements, paving the way toward advanced mechanics.

DOI: 10.1103/PhysRevApplied.18.034006

I. INTRODUCTION

With continuous development and wide popularization of advanced manufacturing processes, micromechanical resonators have become the core components in various fields [1,2]. Under the combined influence of the scale effect and physical fields, micromechanical resonators can easily step into nonlinear states, making their dynamic responses more complicated. In this case, resonators exhibit a wealth of physical characteristics, effectively expanding their applications in timing, sensing, information processes, and quantum sciences [3–8]. Understanding and manipulating these interesting effects has special significance in further improving the micromechanical resonators' performance.

The modal coupling effect is a typical product of nonlinear micromechanical resonators, attracting attention from many research groups in recent years [9–14]. In this case, the independence between eigenmodes is broken, and they interact mutually to produce energy exchange between coupled modes. Recent studies have analyzed the interaction between coupled modes with the same nonlinear characteristics in a single device [2], as well as interactions between different resonators [15,16]. In contrast, the electrostatic parametric coupling mechanism between different nonlinear modes inside a single resonator deserves further exploration.

Here, the electrostatic dispersive resonance modulation is analyzed theoretically and experimentally. A capacitive micromechanical resonator with oblique beams is specially designed as the experimental device, the different modes of which exhibit different nonlinearities. It provides a platform to first realize the coexistence of the bending-induced nonlinearity and electrostatic nonlinear parametric coupling in a single micromechanical resonator. Previous studies have found that the existence of oblique beams will bring the resonator into the stiffness-hardening state, while the capacitive driving method will introduce the stiffness-softening effect [17,18]. As a result, this resonator

*liqingsong12@nudt.edu.cn
†dingbangxiao@nudt.edu.cn

associating with oblique beams and the electrostatic field brings the possibility of different modes exhibiting different nonlinear characteristics.

II. STRUCTURAL DESCRIPTION

The core structure of the resonator is composed of oblique beams, masses, anchors, and a stress-released structure, as shown in Fig. 1(a). The effective length of the oblique beams is 250 μm. A variety of advanced micro- and nanomanufacturing processes are applied in its fabrication processing, including wet etching, dry etching, and silicon-silicon bonding. Additionally, the wafer-level packaging process is used to maintain a vacuum environment (0.5 Pa). Different modal vibration properties of the resonator obtained by the finite-element simulations are displayed in Fig. 1(b). In this work, two modes with different vibration characteristics are selected. These two modes represent two different motions, namely, out-of-plane torsional motion and in-plane bending motion. The coexistence of mechanical nonlinearity and electrostatic

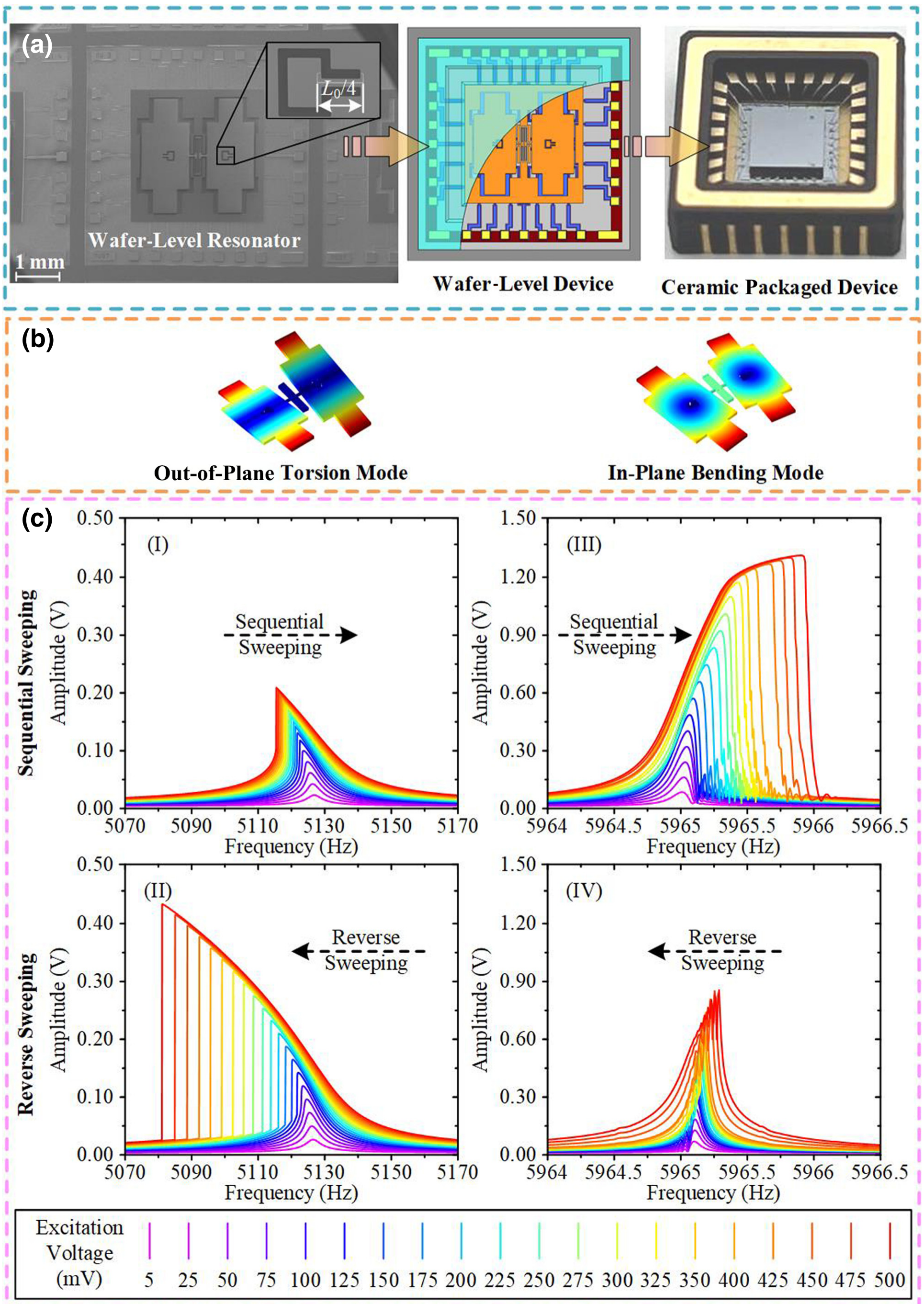

FIG. 1. Resonator's basic characteristics. (a) SEM image and schematic diagram of the resonator. (b) Modal simulation results. (c) Resonator's frequency response. (I),(II) Out-of-plane torsion modal frequency responses under sequential sweeping and reverse sweeping signals, respectively. Obviously, the out-of-plane torsion mode sustains a typical negative Duffing nonlinearity mainly induced by electrostatic forces, resulting in a blueshifting of its resonance (resonant frequency migrates to lower region). (III),(IV) In-plane bending modal frequency responses under sequential sweeping and reverse sweeping signals, respectively. In this case, the in-plane bending mode exhibits a positive Duffing nonlinearity mainly induced by its bending stress, resulting in a redshifting of its resonance (resonant frequency migrates to higher region).

nonlinearity is caused by the bending stress and electrostatic forces, respectively, and they jointly affect the operating modal nonlinear characteristics. The final manifestation of the operating modal nonlinearity is consistent with its dominant nonlinearity. Probing the out-of-plane torsion mode in this configuration reveals the fundamental mode $\omega_t/2\pi = 5127$ Hz with a quality factor of $Q_t \approx 7524$ and similarly the in-plane bending mode is $\omega_b/2\pi = 5965$ Hz with a quality factor of $Q_b \approx 14\,561$. With increasing actuation voltages, resulting in larger motional amplitudes, both modes develop the well-known Duffing nonlinearity. Due to the special structural design, two selected modes exhibit different nonlinear properties: for the out-of-plane torsion mode, its tension-induced nonlinearity is less than the stiffness softening caused by electrostatic forces, so it presents an electrostatic nonlinearity, as shown in Figs. 1(c-I) and 1(c-II); on the contrary, for the in-plane bending mode, the beam's bending deformation cannot be ignored and dominates in its nonlinear region [19], enabling it to exhibit a typical mechanical nonlinearity, as shown in Figs. 1(c-III) and 1(c-IV).

In this resonator, both modes can be independently probed and detected via the modulated resonant signals on the front-end circuits, as discussed in the Supplemental Material [20]. The excitation and detection of these two modes can be achieved through a reasonable electrode configuration. The schematic diagram of the circuits is illustrated in Fig. 2. A lock-in amplifier (Zurich HF2LI) is used to activate and detect the coupled modes simultaneously, and the resonator is placed in a constant-temperature chamber [(303.15 ± 0.1) K] to reduce temperature drift.

Due to the existence of the oblique beam, it is convenient to generate coupling between the in-plane and out-of-plane motions of the resonator. Under the impact of the oblique beam, there is a spindle azimuth angle, θ_p, and it can produce the motions in the in-plane direction and the out-of-plane direction simultaneously. Therefore, the in-plane bending mode also generates the corresponding normal vibration components, as depicted in Fig. 3(a). Considering the symmetry of the topology, the single-side resonant structure is taken as the object (the other side has the same result), and the bending center of the support beam is taken as the origin to establish a spatial coordinate system. According to the spatial geometry relationship, when the bending angle of the oblique beam is ϕ_b and the torsional angle is ϕ_s, the spatial displacement of the resonant structure at any point (x, y, z) on the selected side can be expressed as

$$\begin{bmatrix} \Delta x \\ \Delta y \\ \Delta z \end{bmatrix} = \begin{bmatrix} -\phi_b(\sin\ \theta_p y + \cos\ \theta_p z) \\ \phi_b \sin\ \theta_p x - \phi_s z \\ \phi_b \cos\ \theta_p x + \phi_s y \end{bmatrix}. \tag{1}$$

However, due to the existence of machining errors, the orthogonal coupling error appears in the in-plane bending mode. Compared with the ideal case, its displacement in the normal direction is not symmetrical along the central axis of the structure, as shown in Fig. 3(b). When the orthogonal axis declination is θ_ω, the resonant structure's displacement in the normal direction can be updated as

$$\Delta z = \phi_b \cos\ \theta_p (\sin\ \theta_\omega y + \cos\ \theta_\omega x) + \phi_s y. \tag{2}$$

At this time, the displacement of the resonant structure in the normal direction is no longer asymmetrically distributed, and the resulting changes in the system's potential energy cannot cancel each other out. The electrostatic modal coupling effect can be derived from the superposition of modal vibrations and the system's electrostatic potential energy. When these two modes are actuated

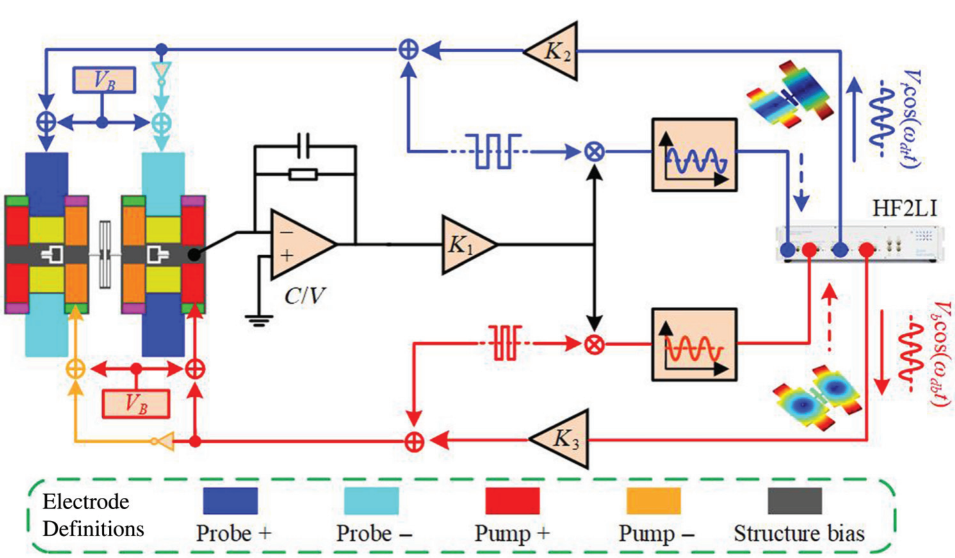

FIG. 2. Schematic circuit of the resonator.

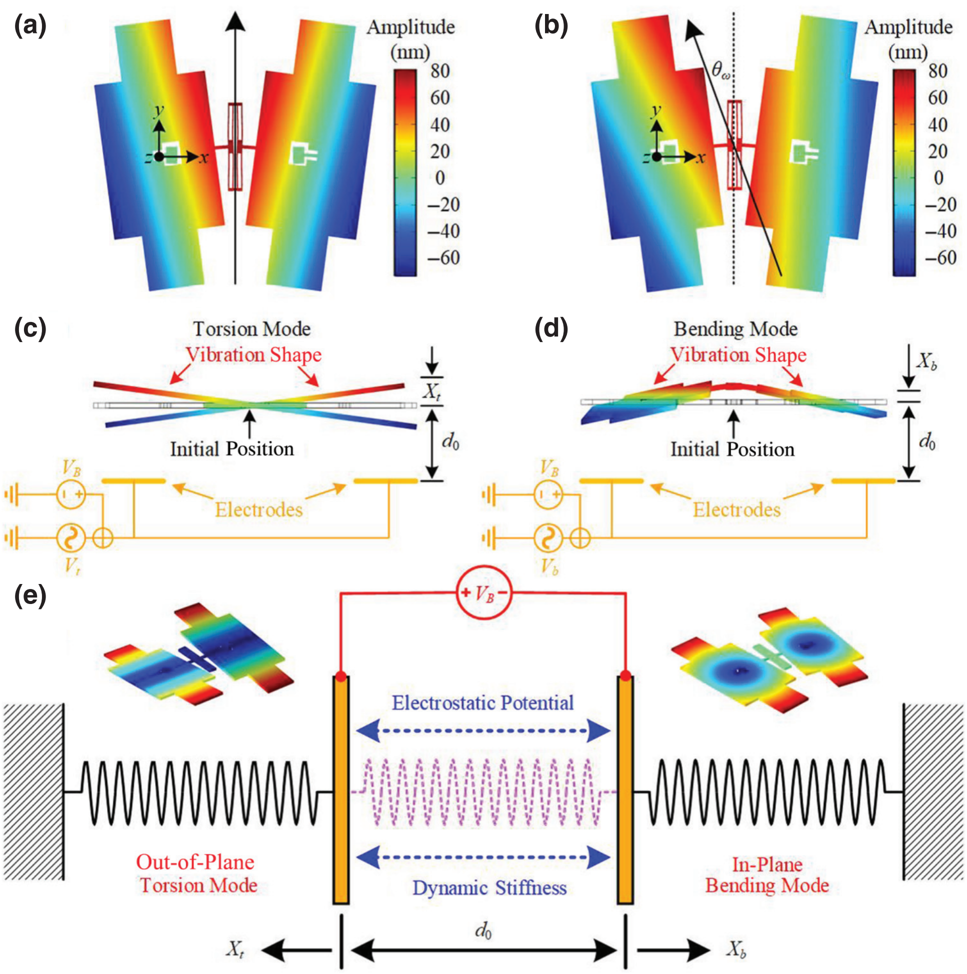

FIG. 3. Schematic diagram of electrostatic coupling. (a) Ideal normal displacements of the in-plane bending mode. (b) Normal displacements of the in-plane bending mode with orthogonal coupling error. (c),(d) Schematic transient pattern of the independently actuated mode. (e) Schematic transient pattern of the electrostatic coupling model.

alone, as shown in Figs. 3(c) and 3(d), the resonant structure with a dc bias voltage, V_B, and electrodes with an ac excitation voltage, V_A, form a capacitor, which is a typical single degree of freedom (1-DOF) system. In this 1-DOF system, due to $V_B \gg V_A$, the electrostatic potential can be expressed as $U_i = -A_i\varepsilon_r V_B^2/2(d_0 + X_i)$. Here, X_i represents the normal displacement of mode i. When these modes are actuated simultaneously, their displacements are superposed together, making the normal displacement of the resonator structure become $d_0 + X_t + X_b$. The system's total electrostatic energy can be expressed as $U = -\sum A_i\varepsilon_r V_B^2/2(d_0 + X_t + X_b)$. As a result, the nonlinear electrostatic parametric coupling can be represented by a two-mechanical-oscillator coupling model [2], as shown in Fig. 3(d). In this model, two coupled mechanical oscillators share a common capacitor with a constant bias voltage, perfectly matching the situation that two individual normal modes share the same resonant structure. The vibration of one mode will change the gap of the shared capacitor and affect the system's potential energy. Meanwhile, the vibration information will be transmitted to the other mode through the shared structure, thereby changing the vibration characteristics of the other mode. Hence, the superposition of coupled modal vibration information can be represented by the modulation of the shared capacitor gap.

III. ELECTROSTATIC COUPLING THEORY

The effective mass, stiffness, and oscillation displacement of each mode are represented by m_i, k_i, and X_i, respectively, where $i = b$ or t indicates the mode label. d_0 is the initial capacitance gap at its equilibrium position without modal interactions, and V_B is the bias voltage on the shared resonant structure. The electrostatic parametric coupling is achieved by the energy flow inside the coupled capacitor. The electrostatic potential energy determined by the vibrational displacement of two coupled mechanical modes can be expressed as $U_e = -A\varepsilon_r V_B^2/2(d_0 + X_b + X_t)$. A is the total effective area of the coupled capacitor, and ε_r is the dielectric constant. In addition, when the in-plane bending mode operates in the large-amplitude resonance state, its resonant structure will undergo a geometric nonlinear deformation, introducing a nonlinear elastic restoring potential into the coupled system [17]. The oblique beam is the main location where bending deformation occurs, and its size satisfies the characteristics of the Euler Bernoulli beam [21], so its nonlinear elastic recovery potential is given by $U_r = 3ESL_0X_b^4/256$. Here, E is silicon's Young's modulus; S and L_0 are the cross-section area and initial length of the oblique beam, respectively. Therefore, the energy equation of the coupled system can be expressed as

$$U = \frac{k_tX_t^2}{2} + \frac{k_bX_b^2}{2} - \frac{A\varepsilon_rV_B^2}{2(d_0+X_t+X_b)} + \frac{3ESL_0}{256}X_b^4,$$
$$T = \frac{m_t\dot{X}_t^2}{2} + \frac{m_b\dot{X}_b^2}{2}. \tag{3}$$

Substituting Eq. (3) into the Lagrange equation, the dynamic equations of the coupled system are obtained:

$$m_t\ddot{X}_t + k_tX_t + \frac{A\varepsilon_rV_B^2}{2(d_0+X_t+X_b)^2} = 0,$$
$$m_b\ddot{X}_b + k_bX_b + \frac{A\varepsilon_rV_B^2}{2(d_0+X_t+X_b)^2} + \frac{3ESL_0}{64}X_b^3 = 0. \tag{4}$$

After introducing damping terms and performing a Taylor expansion of nonlinear restoring forces in new equilibrium displacements x_t and x_b, which are discussed in the Supplemental Material [22], the forced motion of the normalized system is given by

$$\ddot{x}_t + \gamma_t\dot{x}_t + \omega_t^2x_t + \alpha_tx_b + \beta_t(x_t+x_b)^2 + \nu_t(x_t+x_b)^3 = \frac{F_t}{m_t}\cos(\omega_{dt}t),$$
$$\ddot{x}_b + \gamma_b\dot{x}_b + \omega_b^2x_b + \alpha_bx_t + \beta_b(x_t+x_b)^2 + \nu_b(x_t+x_b)^3 + \psi_bx_b^2 + \xi_bx_b^3 = \frac{F_b}{m_b}\cos(\omega_{db}t). \tag{5}$$

Here, γ_i and ω_i indicate the damping rate and angular resonant frequency of mode i ($i = t$ or b), considering the electrostatic-negative-stiffness effect. At the new equilibrium position, the equivalent capacitance gap is adapted to d_1, as discussed in the Supplemental Material [23]. In this case, the expressions of the electrostatic parametric coupling parameters induced by the coupled capacitor are $\alpha_i = -A\varepsilon_rV_B^2/m_id_1^3$, $\beta_i = 3A\varepsilon_rV_B^2/2m_id_1^4$, and $\upsilon_i = -2A\varepsilon_rV_B^2/m_id_1^5$. $F_t = 2\varepsilon_rAV_BV_t/d_0^2$ and $F_b = 2\varepsilon_rAV_BV_b/d_0^2$ are the amplitudes of the electrostatic excitation forces, where V_i is the corresponding ac excitation voltage. The dispersive parametric coupling between selected modes is captured by its electrostatic coupling parameters, α_i, β_i, and ν_i, when the electromechanically coupled system is harmonically pumped and probed with force F_i simultaneously. As for the in-plane bending mode, its positive Duffing stiffness coefficients induced by the nonlinear elastic restoring force are defined as $\psi_b = 9ESL_0X_{b0}/64m_b$ and $\xi_b = 3ESL_0/64m_b$. The coupled nonlinear equations can be numerically solved by using the multiscale method [24], as shown in the Supplemental Material [25]:

$$\left(\frac{\Lambda_t|x_t|^3}{4} + \frac{\Pi_t|x_t||x_b|^2}{4} + 2\omega_t\gamma_t|x_t|\sigma_t\right)^2 = \frac{F_t^2}{m_t^2} - \omega_t^2\gamma_t^2|x_t|^2,$$
$$\left(\frac{\Lambda_b|x_b|^3}{4} + \frac{\Pi_b|x_t|^2|x_b|}{4} + 2\omega_b\gamma_b|x_b|\sigma_b\right)^2 = \frac{F_b^2}{m_b^2} - \omega_b^2\gamma_b^2|x_b|^2. \tag{6}$$

Here, $\sigma_i = \omega_{di} - \omega_i/\gamma_t$ is the normalized frequency-detuning coefficient, when the excitation-signal frequency is ω_{di}. The nonlinear coupling coefficients are

$$\Lambda_t \approx -\frac{3\upsilon_t}{\gamma_t^2}, \Pi_t \approx -\frac{6\upsilon_t}{\gamma_t^2},$$
$$\Lambda_b \approx -\frac{3\upsilon_b}{\gamma_t^2} - \frac{3\xi_b}{\gamma_t^2}, \Pi_b \approx -\frac{6\upsilon_b}{\gamma_t^2}. \tag{7}$$

When these modes operate simultaneously in resonance, indicating that their vibration amplitudes reach a maximum, the maximum frequency shift, σ_t, of the torsion mode caused by the resonance of the bending mode and σ_b of the bending mode caused by the resonance of the torsion mode are given by

$$\sigma_t = -\frac{\gamma_t^3}{8\omega_t}\left[\frac{\Lambda_tm_t^2}{\omega_t^2} + \frac{\Pi_tm_b^2\gamma_t^2}{\omega_b^2\gamma_b^2}\right],$$
$$\sigma_b = -\frac{\gamma_t^3}{8\omega_b}\left[\frac{\Lambda_bm_b^2\gamma_t^2}{\omega_b^2\gamma_b^2} + \frac{\Pi_bm_t^2}{\omega_t^2}\right]. \tag{8}$$

Obviously, the response of one mode will modulate the resonant frequency of the other mode, when these modes are activated at the same time. Since these two coupled modes share the same resonant structure, one mode's response will change the dynamic equilibrium position of the coupled capacitor, which changes the dynamic stiffness of the other mode, in turn. Through activating a coupled pump mode, the resonance of the probe mode can be manipulated consequently. The schematic diagram of the resonance modulation based on the modal coupling effect is shown in Figs. 4(a) and 5(a).

IV. SIMULATIONS AND EXPERIMENTS

To ensure the electrostatic coupling strength [2], a stable 9 V dc bias voltage (V_B) is applied on the resonant structure. According to Eq. (8), the resonance modulation range can be adjusted by changing the amplitude of pump signals. Different pump signals generated by the lock-in

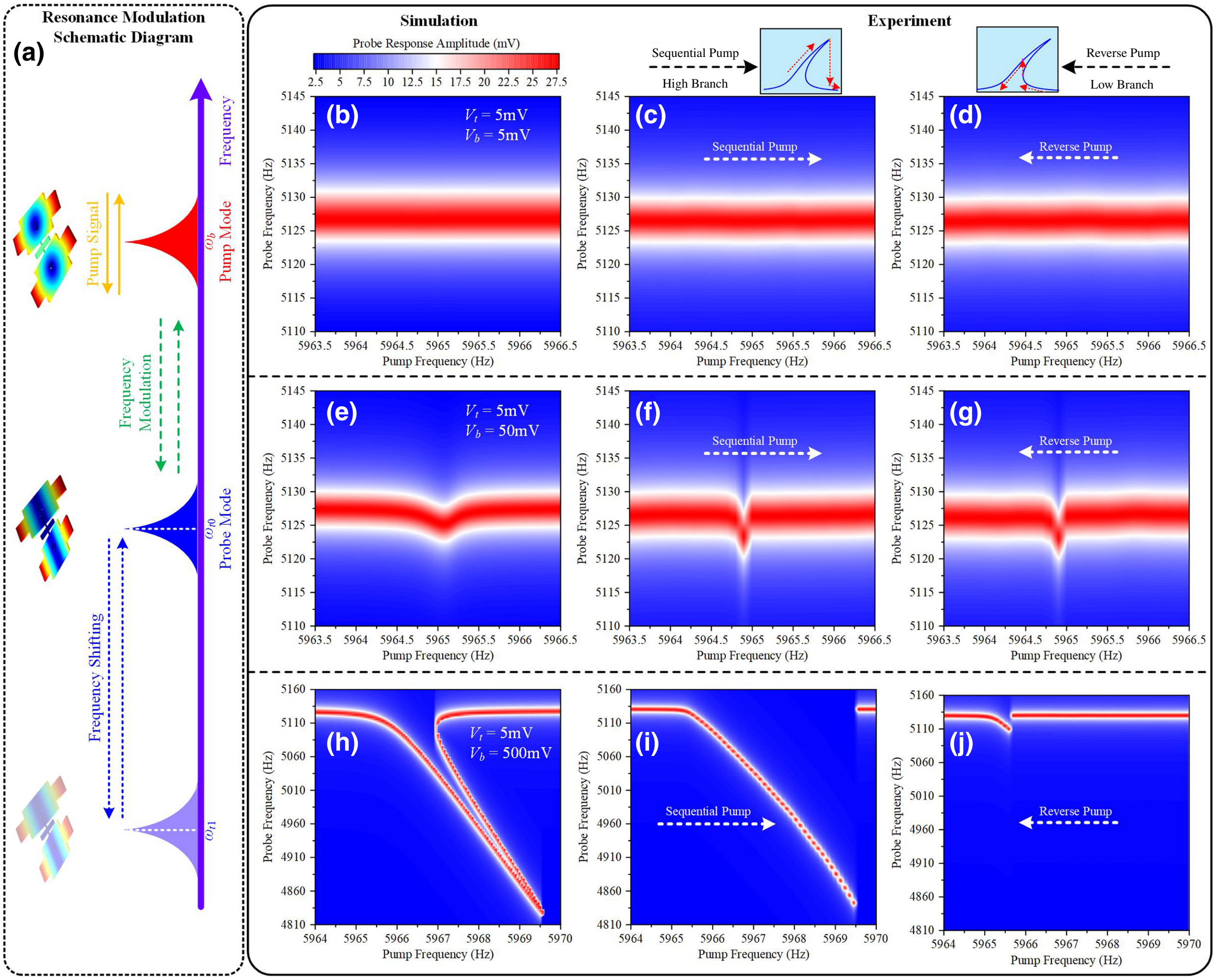

FIG. 4. Resonance modulation of the out-of-plane torsion mode. (a) Schematic diagram. (b)–(d) Dispersive frequency responses when both modes are linearly actuated ($V_t = 5$ mV, $V_b = 5$ mV), where (b) indicates the numerical simulation results, and (c) corresponds to the sequential pump (pump frequency changes from low to high) experiments, while (d) corresponds to the reverse pump (pump frequency changes from high to low). (e)–(g) Dispersive frequency responses when the in-plane bending mode is weakly nonlinearly actuated ($V_t = 5$ mV, $V_b = 50$ mV). (h)–(j) Dispersive frequency responses when the in-plane bending mode is strongly nonlinearly actuated ($V_t = 5$ mV, $V_b = 500$ mV).

amplifier are applied on corresponding electrodes to verify the effectiveness of the theorical analysis. The comparison of the simulation results and experimental observations for different probed modes are displayed in Figs. 4 and 5.

Figure 4 exhibits the dispersive modulation of the out-of-plane torsion mode under different in-plane bending modal resonance states. In this case, the out-of-plane torsion mode is steadily probed, while the in-plane bending mode is harmonically pumped at the same time. The numerical simulation results derived from the electrostatic coupling model are displayed in Figs. 4(b), 4(e), and 4(h) with different pump parameters, which is perfectly consistent with experimental observations. When coupled modes both operate in linear response regions with $V_t = V_b = 5$ mV, the modal interaction remains silent, as shown in Figs. 4(b)–4(d). Next, increasing the pump amplitude to make the in-plane bending mode enter its weak nonlinear response range, amplitude-frequency responses of the out-of-plane torsion mode are recorded in Figs. 4(e)–4(g). In this case, electrostatic coupling induced by the larger vibration of the in-plane bending mode begins to appear and causes the dispersive frequency shifting of the out-of-plane torsion mode. However, within the weak nonlinear state range, the nonlinear response of the pump mode is relatively weak, where its response amplitudes under the sequential and reverse sweeping signals are almost the same. Therefore, almost identical frequency-modulation capabilities are observed in Figs. 4(f) and 4(g) with pump signals in different directions. Noticeably, with further enhancement of the pump amplitude, indicating

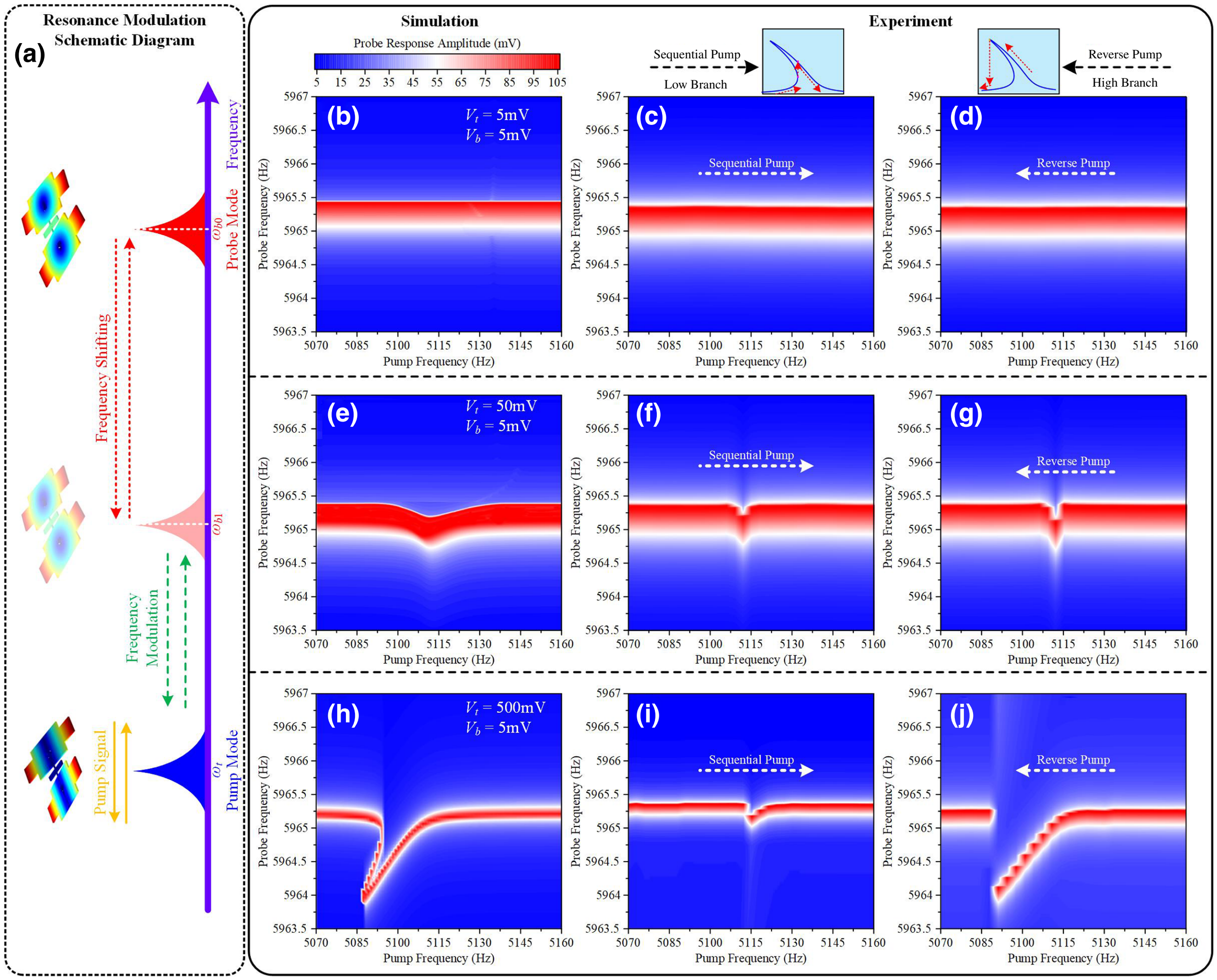

FIG. 5. Resonance modulation of the in-plane bending mode. (a) Schematic diagram. (b)–(d) Dispersive frequency responses when both modes are linearly actuated ($V_t = 5$ mV, $V_b = 5$ mV), where (b) indicates the numerical simulation results, and (c) corresponds to the sequential pump experiments, while (d) corresponds to the reverse pump. (e)–(g) Dispersive frequency responses when the out-of-plane torsion mode is weakly nonlinearly actuated ($V_t = 50$ mV, $V_b = 5$ mV). (h)–(j) Dispersive frequency responses when the out-of-plane torsion mode is strongly nonlinearly actuated ($V_t = 500$ mV, $V_b = 5$ mV).

that the pump mode steps into its strong stiffness-hardening region, the distinct bifurcation of the dispersive frequency modulation appears, as shown in Figs. 4(h)–4(j). Here, the resonance state of the pump mode plays a significant role in dispersive modulation, which can be derived from the difference between the sequential pump and reverse pump. Due to the mechanical nonlinearity, the response of the pump mode (in-plane bending mode) exhibits the high-branch response and low-branch response, corresponding to the sequential excitation and reverse excitation signals, respectively. With the sequential pump, the response of the pump mode is much larger than that of the reverse pump, leading to a larger frequency shifting, as shown in Figs. 4(i) and 4(j). Meanwhile, the hopscotch of resonance modulation appears with the nonlinear bifurcation of the pump mode in the high-frequency region. With the sequential pump, the pump mode can reach a larger amplitude, enhancing the frequency modulation of the probe mode. On the contrary, the pump mode's response is reduced under the reverse pump, weakening the frequency-shifting effect. As a result, the bifurcation and hopscotch of the dispersive resonance modulation is determined by the response of the pump mode.

Similarly, the dispersive modulation of the in-plane bending mode under different out-of-plane torsion modal resonance states is depicted in Fig. 5. Compared with Fig. 4, the only difference is that the pump mode (out-of-plane torsion mode) exhibits typical electrostatic nonlinearity, so its hopscotch appears in the low-frequency region. Based on the analysis above, it is proven that the resonance state of the probe mode can be modulated by the amplitudes and directions of pump signals. Owing to the better damping

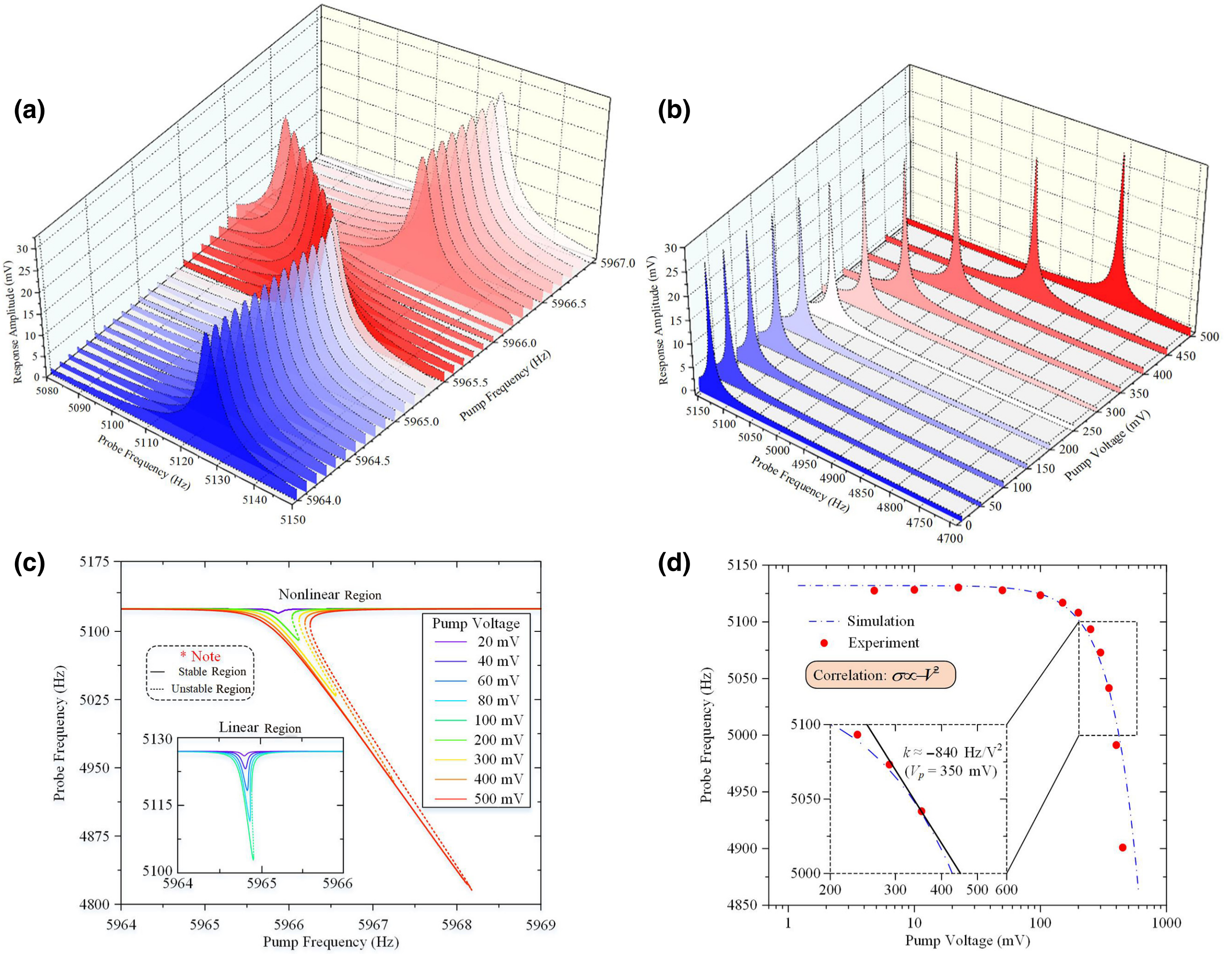

FIG. 6. Influencing factors of the capacitive modal coupling effect. (a) Dispersive frequency shifting under different pump frequencies ($V_b = 150$ mV). (b) Frequency modulation of the probe mode as a function of the pump frequency with different pump amplitudes. (c) Maximum dispersive frequency shifting under different pump amplitudes. (d) Relationship between the frequency shifting and pump amplitude with $\omega_t = 2\pi \times 5120$ Hz, $\gamma_t = 2\pi \times 2.395$, $m_t = 9.374\ \mu$g, and $d_0 = 2\ \mu$m.

rate and linewidth of the out-of-plane torsion mode, its resolution of frequency detection is much better than that of the in-plane bending mode. Thus, this paper focuses on the condition that the out-of-plane torsion is the probe mode, while the in-plane bending mode is the pump mode.

It is observed that the displacement of the pump mode will cause a frequency dispersion of the probe mode in this resonator, which is very similar to the tension-induced parametric interaction that is well known in clamped-clamped beam resonators [26]. The difference is that the frequency of the probe mode will shift to lower values under the electrostatic nonlinear interaction, while the frequency shifts to higher values for the tension-induced nonlinear interaction. The origin of the probe mode's frequency dispersion can be explained in terms of the electrostatic force generated from the pump mode's motion that softens its restoring potential in a mechanism analogous to the Duffing term. The frequency-shifting direction and range are determined by Λ_i and Π_i, which are the reflections of nonlinear elastic coefficients of coupled modes, as discussed in the Supplemental Material [27]. Additionally, the location of the modulation hopscotch is related to the pump mode's nonlinear response. When the pump mode is a mechanical nonlinear mode, the hopscotch appears in the higher-frequency region; when it exhibits an electrostatic nonlinearity, the hopscotch appears in the lower-frequency region.

V. RESULTS AND DISCUSSION

Experiments illustrate a 295.6-Hz frequency shifting under a 500-mV pump signal, presenting great potential for wide-range frequency modulation, nearly 2 orders its bandwidth of 3.1 Hz and a 57 656-ppm pull range from its center frequency. The resonance of the probe mode can be modulated by the vibration of the pump mode (pump amplitude or pump direction). When two modes retain the resonance conditions $|x_t| = F_t/m_t\omega_t\gamma_t$ and $|x_b| = F_b/m_b\omega_b\gamma_b$, the relationship between the probe modal frequency shifting and the pump voltage can be obtained from Eq. (6), as analyzed in the Supplemental Material [28]:

$$\sigma_t = -\frac{\Pi_t \Gamma_b}{8\omega_t\gamma_t} V_b^2 - \Delta_t o. \tag{9}$$

The measurement results shown in Fig. 6 reveal that the probe mode's frequency shifting is captured by the pump mode's response and is proportional to its pump voltage squared, as shown in Eq. (9). Additionally, the sensitivity of this dispersive electrostatic transduction is given by

$$S = -\frac{\Pi_t \Gamma_b}{8\omega_t\gamma_t} = -\frac{3\varepsilon_r^3 A^3}{\pi m_t\omega_t\gamma_t} \frac{V_B^4}{m_b^2\omega_b^2\gamma_b^2 d_0^9}. \tag{10}$$

As for the resonator in this work, it is about 1200 Hz/V^2, revealing that a 1-V pump voltage yields a 1200-Hz frequency shift; in other words, this voltage-induced frequency shift is 3 orders of the pump voltage, presenting great potential for wide-range precise frequency modulation. Based on the modal coupling effect, it demonstrates an efficient voltage-frequency transduction scheme that is different from the traditional electrostatic modulation method widely used in frequency reference devices [29], such as voltage-controlled oscillators (VCO). In this case, its pull range is about 23.4% for only 1-V pump voltage, which is significantly larger than previously reported results (4%–20.2%) using *LC*-tank-based VCOs [30–32]. Compared with these conventional electrostatic modulation methods, the dispersive frequency modulation presents a squared output relationship, as shown in Eq. (9), and allowing it to remarkably increase the pull range while keeping its small size and low cost by using MEMS resonators with low phase noise. Moreover, it is worth noting that the modulation sensitivity and range can be controlled and flexibly designed according to different requirements, effectively expanding its application fields.

VI. CONCLUSION

A capacitive resonator with different nonlinear modes is specially designed to analyze the electrostatic dispersive coupling. Two coupled modal oscillations superpose and their resonance can be modulated by the electrostatic negative stiffness induced by the other mode's displacement. The dispersive coupling between intrinsic modes enables the probe resonance to be tuned by nearly 100 times its bandwidth, and its range and polarity can also be controlled by selecting the resonance of the pump mode. It is demonstrated to be an effective resonance modulation method and a highly sensitive and wide-range voltage-frequency transduction scheme, which is totally different from its existing counterpart based on electrostatic modulation. Its sensitivity exhibits a great potential of nearly 3 orders of its pump voltage and can be customized to satisfy different requirements. It expands the pull range more than 23% with promising potential for application in VCOs. This simple coupled electromechanical resonator paves the way toward actively engineered mechanics where nonlinear phenomena can be applied to high-precision sensing and quantum calculations, which is meaningful for enhancing the performance of MEMS resonators.

See the Supplemental Material [33] for detailed descriptions of the resonator's structure, processing, and experimental sets. The expansion of the electrostatic parametric coupling system in the multiscale used to generate the numerical solutions are also analyzed in detail.

ACKNOWLEDGMENTS

The authors would like to thank the Laboratory of Microsystem, National University of Defense Technology, China, for equipment access and technical support. This work is supported by the National Key Research and Development Program of China (Grant No. 2018YFB2002304), the National Natural Science Foundation of China (Grant No. 62104258), and the Excellent Youth Foundation of Hu'nan Scientific Committee (Grant No. 2020JJ2033).

[1] Z. Wang, H. Jia, X. Zheng, R. Yang, G. Ye, X. Chen, and P. X. Feng, Resolving and tuning mechanical anisotropy in black phosphorus via nanomechanical multimode resonance spectromicroscopy, Nano Lett. **16**, 5394 (2016).

[2] X. Zhou, C. Zhao, D. Xiao, J. Sun, G. Sobreviela, D. D. Gerrard, Y. Chen, I. Flader, T. W. Kenny, X. Wu, and A. A. Seshia, Dynamic modulation of modal coupling in microelectromechanical gyroscopic ring resonators, Nat. Commun. **10**, 4980 (2019).

[3] E. Ng, *et al.*, in *The long path from MEMS resonators to timing products, IEEE MEMS* (2015).

[4] X. Zou, P. Thiruvenkatanathan, and A. A. Seshia, A seismic-grade resonant MEMS accelerometer, J. Microelectromech. Syst. **23**, 768 (2014).

[5] S. K. Roy, V. T. Sauer, J. N. W. Bachman, A. Venkatasubramanian, and W. K. Hiebert, Improving mechanical sensor performance through larger damping, Science **360**, 6394 (2018).

[6] J. Sun, W. Yang, T. Zheng, X. Xiong, Y. Liu, Z. Wang, Z. Li, and X. Zou, Novel nondelay-based reservoir computing with a single micromechanical nonlinear resonator for high-efficiency information processing, Microsyst. Nanoeng. **7**, 83 (2021).

[7] D. Hatanaka, I. Mahboob, and H. Yamaguchi, Phonon waveguides for electromechanical circuits, Nat. Nanotechnol. **9**, 520 (2014).

[8] R. Riedinger, A. Wallucks, I. Marinković, C. Löschnauer, M. Aspelmeyer, S. Hong, and S. Gröblacher, Remote quantum entanglement between two micromechanical oscillators, Nature **556**, 473 (2018).

[9] Y. Tsaturyan, A. Barg, E. S. Polzik, and A. Schliesser, Ultracoherent nanomechanical resonators via soft clamping and dissipation dilution, Nat. Nanotechnol. **12**, 776 (2017).
[10] H. J. R. Westra, M. Poot, H. S. J. van der Zant, and W. J. Venstra, Nonlinear Modal Interactions in Clamped-Clamped Mechanical Resonators, Phys. Rev. Lett. **105**, 117205 (2010).
[11] C. Zhao, M. H. Montaseri, G. S. Wood, S. H. Pu, A. A. Seshia, and M. Kraft, A review on coupled MEMS resonators for sensing applications utilizing mode localization, Sens. Actuators, A **249**, 93 (2016).
[12] M. H. Matheny, L. G. Villanueva, R. B. Karabalin, J. E. Sader, and M. L. Roukes, Nonlinear mode-coupling in nanomechanical systems, Nano Lett. **13**, 1622 (2013).
[13] X. Wei, T. Zhang, Z. Jiang, J. Ren, and R. Huan, Frequency latching in nonlinear micromechanical resonators, Appl. Phys. Lett. **110**, 143506 (2017).
[14] H. Zhang, J. Huang, W. Yuan, and H. Chang, A high-sensitivity micromechanical electrometer based on mode localization of two degree-of-freedom weakly coupled resonators, J. Microelectromech. Syst. **25**, 937 (2016).
[15] I. Mahboob, N. Perrissin, V. N. K. Nishiguchi, D. Hatanaka, Y. Okazaki, A. Fujiwara, and H. Yamaguchi, Dispersive and dissipative coupling in a micromechanical resonator embedded with a nanomechanical resonator, Nano Lett. **15**, 2312 (2015).
[16] I. Mahboob, V. N. K. Nishiguchi, A. Fujiwara, and H. Yamaguchi, Multi-mode parametric coupling in an electromechanical resonator, Appl. Phys. Lett. **103**, 153105 (2013).
[17] K. Lu, X. Zhou, Q. Li, K. Wu, Y. Zhang, M. Zhuo, X. Wu, and D. Xiao, in *A wide range frequency coherent modulation control based on modal coupling effect in MEMS resonators, IEEE MEMS* (2021).
[18] C. Chen, D. H. Zanette, D. A. Czaplewski, S. Shaw, and D. López, Direct observation of coherent energy transfer in nonlinear micromechanical oscillators, Nat. Commun. **8**, 15523 (2017).
[19] T. Miao, X. Zhou, F. Ou, K. Lu, Y. Zhang, X. Wu, and D. Xiao, in *Energy Transfer Control of Mode Cooling Induced by Capacitive Nonlinear Coupling in MEMS Resonator, IEEE MEMS* (2019).
[20] See the Supplemental Material at http://link.aps.org/supplemental/10.1103/PhysRevApplied.18.034006 for the experimental front-end circuits.
[21] R. Kashyap, T. R. Lenka, and S. Baishya, Distributed parameter modeling of cantilevered-d_{33}-mode piezoelectric energy harvesters, IEEE Trans. Electron Devices **63**, 1281 (2016).
[22] See the Supplemental Material at http://link.aps.org/supplemental/10.1103/PhysRevApplied.18.034006 for details about the modeling of the dynamic normalized system.
[23] See the Supplemental Material at http://link.aps.org/supplemental/10.1103/PhysRevApplied.18.034006 for a definition of the new equilibrium position.
[24] A. Nayfeh and D. Mook, *Nonlinear oscillations* (Wiley, New York, 1979).
[25] See the Supplemental Material at http://link.aps.org/supplemental/10.1103/PhysRevApplied.18.034006 for details about the multiple timescale processing.
[26] H. Okamoto, A. Gourgout, C. Y. Chang, K. Onomitsu, I. Mahboob, E. Y. Chang, and H. Yamaguchi, Coherent phonon manipulation in coupled mechanical resonators, Nat. Phys. **9**, 480 (2013).
[27] See the Supplemental Material at http://link.aps.org/supplemental/10.1103/PhysRevApplied.18.034006 for details about the nonlinear coupling coefficients.
[28] See the Supplemental Material at http://link.aps.org/supplemental/10.1103/PhysRevApplied.18.034006 for details about the influence of the pump voltage.
[29] R. I. Ruslan, T. Satoh, and T. Akitsu, Voltage-controlled narrowband and wide, variable-range four-segment quartz crystal oscillator, IEEE Trans. Ultrason. Ferroelectr. Freq. Control **59**, 564 (2012).
[30] F. Zhao and F. F. Dai, A 0.6-V quadrature VCO with enhanced swing and optimized capacitive coupling for phase noise reduction, IEEE Trans. Circuits Syst. I **59**, 1694 (2012).
[31] H. Ryu, K. W. Ha, and D. Baek, Low-power quadrature voltage-controlled oscillator using current-reuse and transformer-based Armstrong topologies, Electron. Lett. **52**, 462 (2016).
[32] E. Turkmen, O. Ceylan, H. B. Yagci, and M. Kartal, The X(-Band) files: An X-band microstrip voltage-controlled oscillator with wideband tuning range, IEEE Microw. Mag. **17**, 88 (2016).
[33] See the Supplemental Material at http://link.aps.org/supplemental/10.1103/PhysRevApplied.18.034006 for descriptions of the resonator's structure, processing, and experimental sets.